Supporting Information

Single-molecule strong coupling at room temperature in individual plasmonic nanocavities

Rohit Chikkaraddy[1], Bart de Nijs[1], Felix Benz[1], Steven J. Barrow[2], Oren A. Scherman[2], Edina Rosta[3], Angela Demetriadou[4], Peter Fox[4], Ortwin Hess[4], and Jeremy J. Baumberg[1*]

[1] NanoPhotonics Centre, Cavendish Laboratory, University of Cambridge, Cambridge, CB3 0HE, UK

[2] Melville Laboratory for Polymer Synthesis, Department of Chemistry, University of Cambridge, Lensfield Road, Cambridge CB2 1EW, UK

[3] Department of Chemistry, King's College London, London SE1 1DB, United Kingdom

[4] Blackett Laboratory, Department of Physics, Prince Consort Road, Imperial College, London, SW7 2AZ, UK

[*]corresponding author: jjb12@cam.ac.uk

Methods:

Sample preparation:

Gold substrates on silicon wafers are coated using electron-beam-evaporation of a 70 nm thick gold layer on a 5 nm chrome adhesive layer. The surface roughness of the film is minimised by choosing a slow evaporation rate of 0.1 A s^{-1}. The gold coated substrate is submerged in a 1 mM solution of CB[7] in de-ionized water overnight to deposit a layer of CB[7] molecules or CB[7]-MB complexes. The 40-60 nm citrate capped gold nanoparticles (from BBI, used as received) are drop cast onto the coated film where physisorption takes place and are rinsed off with de-ionized water after 10 s to remove excess particles. The substrate is then blown dry using nitrogen.

Spectroscopy:

Optical dark field spectra were recorded on a modified Olympus BX51 microscope. Samples are illuminated with a focused white light (halogen) source at 55^0. The scattered light is collected through a 100× dark field objective (NA=0.8) and routed to a fiber-coupled (50µm optical fiber) TEC-cooled Ocean Optics cooled spectrometer. We use a standard diffuser as a reference to normalise the white light scattering. Raman spectroscopy uses a Renishaw InVia system coupled to a 633 nm laser. The laser power is 0.35 mW and integration times are 10 s.

FDTD simulation:

The electromagnetic response of the nanoparticle on mirror geometry (NPoM) is simulated by 3-dimensional finite difference time domain (FDTD) calculations using Lumerical FDTD Solutions v8.9. The structure is modelled as a gold sphere of 40 – 60 nm diameter on top of

a gold layer, with a flat infinite 1nm thick dielectric sheet in between. The dielectric sheet has real refractive index varied between 1.0 and 1.8. The gold nanoparticle was illuminated with *p*-polarized plane waves from an angle of incidence of $\theta_i = 55°$. The scattered light was then collected within a cone of half-angle $\theta_c = 53°$, based on the numerical aperture of the objective.

S1: Methylene blue (MB) encapsulated in Cucurbit[7]uril:

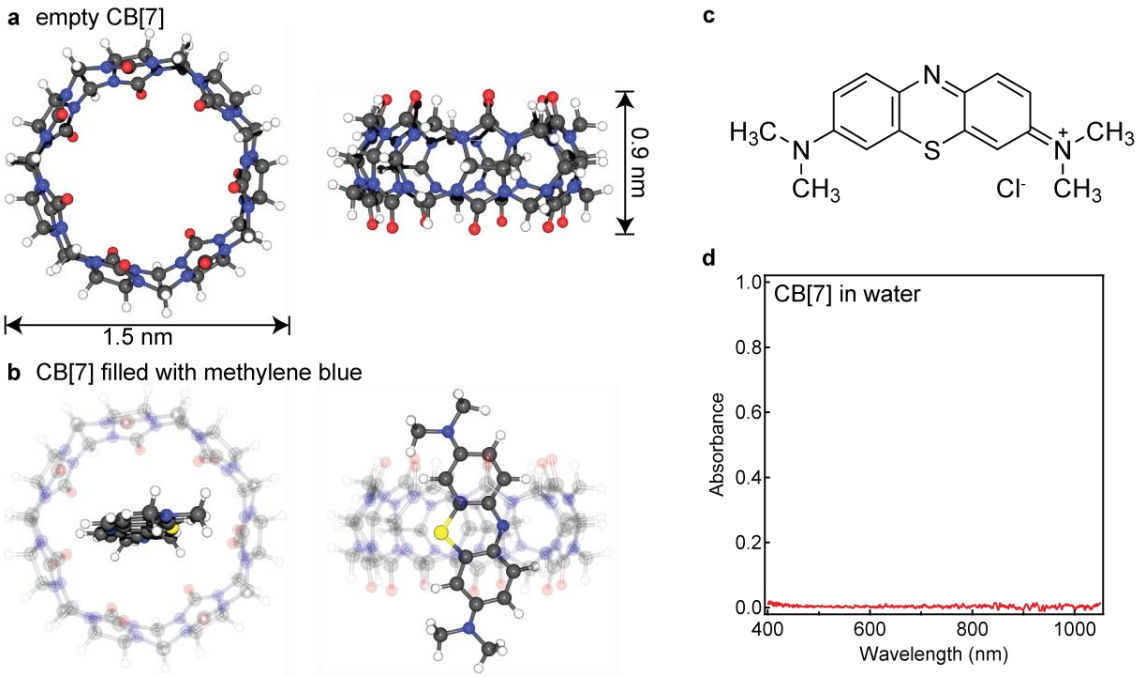

Figure S1 | Encapsulation of MB inside CB[7]. a, Top and side view of CB[7] unfilled. **b,** Top and side view of MB encapsulated in CB[7]. **c**, Chemical structure of MB. **d,** Absorption spectrum of CB[7] in water.

The CB[7] binds to Au with the carbonyl portals at either end of the barrel structure flat to the metal surface[7]. Dye molecules such as MB when outside CB invariably bind flat to the metal substrate in the orthogonal orientation (main paper ref [20]).

S2: Nanoparticle size variation:

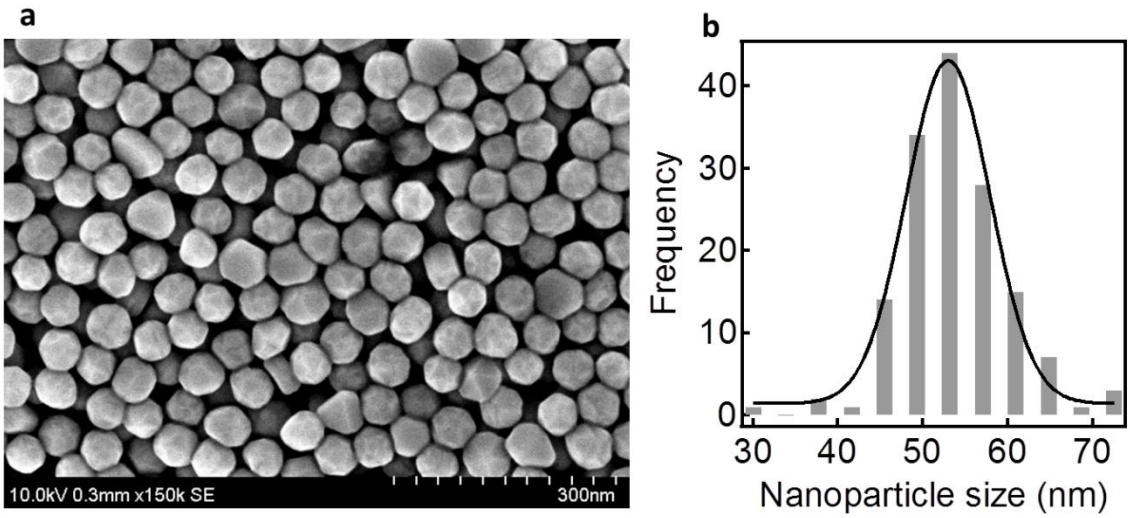

Figure S2 | Size distribution of Au nanoparticles. a, Scanning electron microscope image of drop cast Au NPs, together with **b,** statistics of average nanoparticle diameters used in one set of experiments.

S3: 3D FDTD simulations for strong coupling

FDTD simulations are performed to calculate the scattering spectrum from 40 nm spherical Au nanoparticle placed 1 nm above the thick Au mirror in the presence of dye in the gap. The dye molecules are modelled as a 1 nm thick dispersive medium in the gap with the dielectric permittivity described by the Lorentz model as

$$\varepsilon_{tot}(\omega) = \varepsilon_{\infty} + \frac{f\omega_0^2}{\omega_0^2 - \omega^2 - i\gamma_0\omega}$$

Here $\varepsilon_{\infty} = 1.96$ is the high-frequency component, $f = 0.27$ is the reduced oscillator strength, $\hbar\omega = 1.86$ eV is the exciton transition energy and $\gamma_0 = 85$ meV is the exciton line width.

The calculated scattering spectra are compared with experimental results (Figure S2). The simulated spectrum matches the experimental results not just in peak positions, but also in the ratio between the peaks and the spectral dip, within an experimental error of 5% which arises from variations of nanoparticle size and other uncontrolled geometrical parameters. In simulations we also observe a shoulder peak at the absorption maxima of the dye, due to scattering from dye components which do not participate in strong coupling. The lack of shoulder peak at 665 nm in experiment implies the participation of all dye molecules in strong coupling.

Near-field $|\boldsymbol{E}|$ maps are simulated at ω_+(595 nm), ω_0(665 nm) and ω_-(756 nm) (Fig. S2c). Near-field profiles at ω_+(595 nm) and ω_-(756 nm) are similar to the gap mode of the NPoM with a maximum $|\boldsymbol{E}|$ at the centre of the junction between nanoparticle and mirror. In

contrast to this, at the dye resonance ω_0(665 nm) the $|\boldsymbol{E}|$ field shows a minimum around the junction between nanoparticle and mirror, which corresponds to enhanced conductance[1] of excitons due to strong coupling.

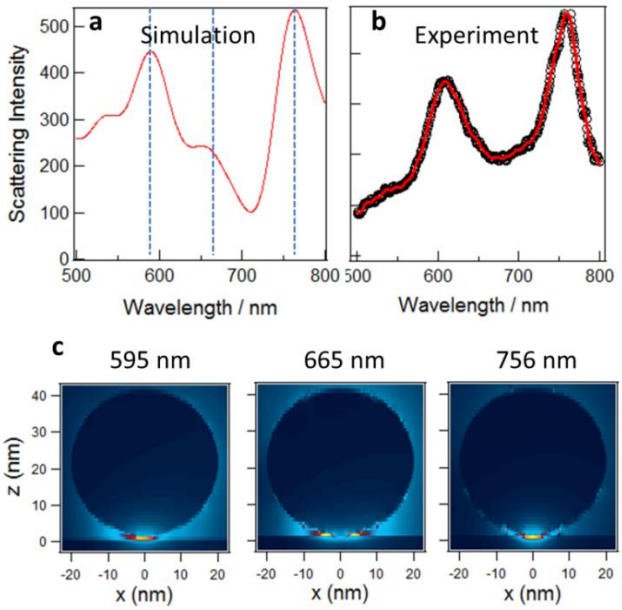

Figure S3 | 3D finite-difference time-domain (FDTD) simulations. a, FDTD simulated scattering spectrum from NPoM geometry with Lorentz absorbing material. **b,** Experimentally obtained scattering spectrum. **c,** Simulated near-field |E| map at ω_+(595 nm), ω_0(665 nm) and ω_-(756 nm) [blue dashed in (a)].

S4: Scattering spectra with different dipole orientation of MB

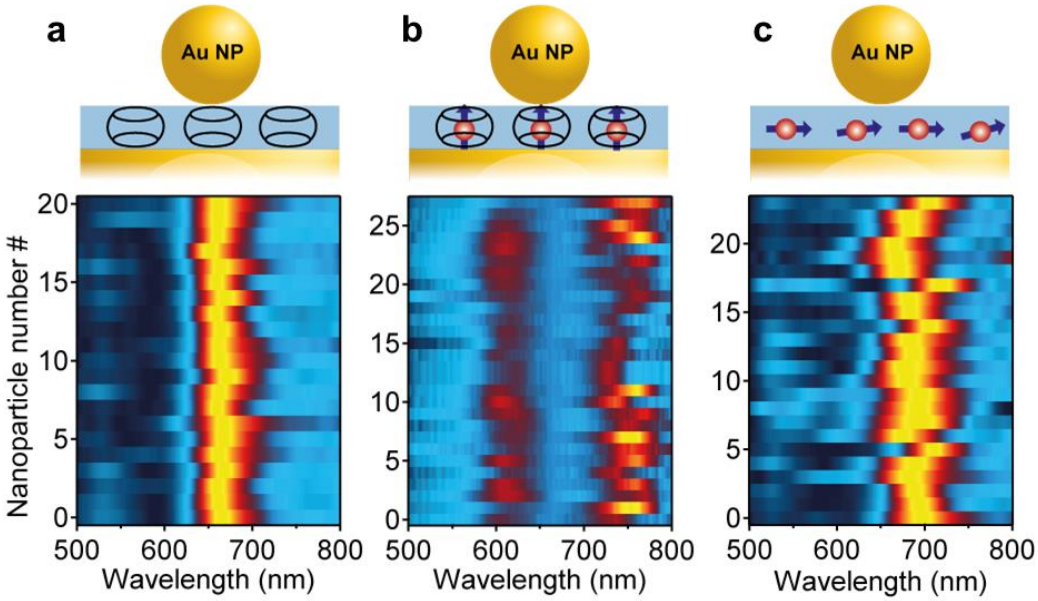

Figure S4 | Strong coupling seen in scattering spectra of individual NPoMs. a-c, Comparison of scattering spectra from different NPoMs (schematics above), with gaps filled by monolayer of CB[7] (a) without, and (b) with, encapsulated MB dye molecules, (c) MB molecules lying flat on substrate without encapsulating CB[7].

S5: Simulated scattering spectra from 40-60 nm particles in NPoMs

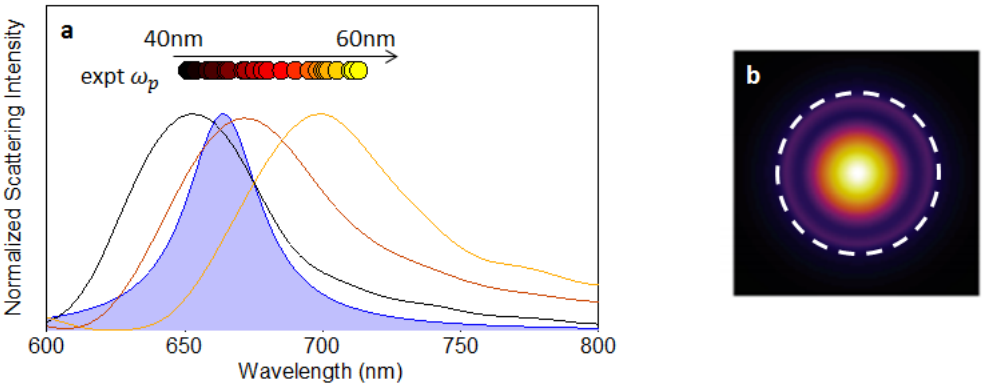

Figure S5 | a, Simulated scattering spectra from 40-60 nm particles in NPoMs. FDTD simulated scattering spectra of 40 (black), 50 (red) and 60 nm (orange) nanoparticles in NPoM. Absorption resonance of single MB shaded blue. Circles in legend are the experimentally extracted coupled plasmon resonance (ω_p). b, In-plane vertical field distribution in the middle of the gap, 10nm facet marked as white dashed.

The NPoM construct has been studied extensively over the past few years, and combines a number of useful properties. In the small nano-gap regime studied here, the dominant modes emitting light up to λ <1000nm have vertical field orientation in the gap, and are mixtures of antennae modes spread across the entire nanoparticle and cavity modes tightly confined within the gap.[2,3] This allows the small effective wavelength ($\sim \lambda_0/100$) cavity modes to couple into the far field through the mode matching antenna modes. The modes seen here radiate at high angle (around 60° to the normal), entirely controlled by the vertical field orientation in the gap and the NPoM geometry. Different shaped nanoparticles have different coupling into the far field, and we concentrate on near-spherical nanoparticle structures which we have shown are most efficiently accessed for such small gaps[3]. In such small 40nm nanoparticles used here, the facets are 5-10nm and do not strongly affect the lateral field distributions, which are confined to the central region of the facet (Fig.S5b).

S6: Calculation of mode volume and mean number of molecules

Two independent methods are used to quantify the mode volume.

Method I: A standard Purcell factor calculation looks at the spontaneous emission rate of a classical dipole in the plasmonic cavity. We use finite difference time domain (FDTD) simulations to extract this emission rate as well as to quantify the cavity Q factor. A typical simulation for 40nm Au NPs spaced 0.9nm above a Au surface embedded in refractive index 1.4, gives a spectrum for the spontaneous emission rate as in Fig.S6.

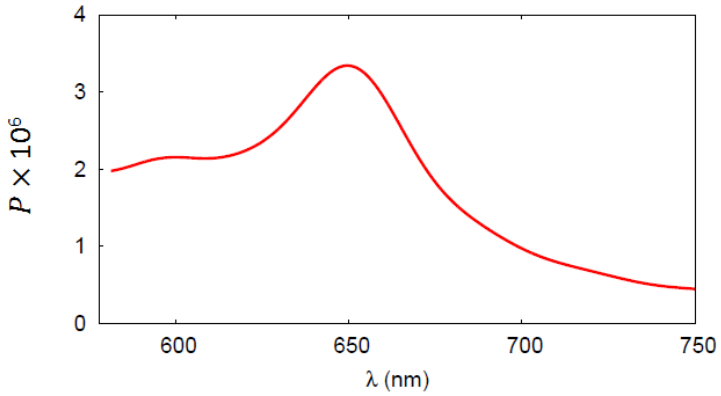

Figure S6 | Purcell Factor (P). FDTD simulation of NPoM with classical emitter placed in the centre of the gap at the position of maximum field, and spontaneous emission rate plotted as a function of wavelength.

Since the Purcell factor is defined as

$$P = \frac{3}{4\pi^2}\left(\frac{\lambda_0}{n}\right)^3 \frac{\mathrm{Q}}{V} \tag{S1}$$

and we can calculate the Q factor, here Q=15.9±0.5 at 646 nm, so we can then extract a cavity volume. We thus find the effective mode volume at 646 nm is V=35.9 nm^3.

Method II: FDTD simulations excite the plasmonic cavity and the electromagnetic mode energy density is used to derive a mode volume. We excite the structure with a plane wave incident on the plasmonic structure at 90°, which excites the plasmonic resonance in a similar fashion as the experiment. The energy density of the system is given by:

$$W(\boldsymbol{r},\omega) = \frac{1}{2}\left(\frac{\partial[\,\omega\,\varepsilon(\boldsymbol{r},\omega)]}{\partial\omega}\,\varepsilon_0\,|E(\boldsymbol{r},\omega)|^2 + \mu_0\,|H(\boldsymbol{r},\omega)|^2\right) \tag{S2}$$

Since the permittivity $\varepsilon(\boldsymbol{r},\omega)$ of gold is dispersive and negative at optical frequencies, one needs to use the term $\frac{\partial[\,\omega\,\varepsilon(\boldsymbol{r},\omega)]}{\partial\omega}$ to correctly calculate W. Otherwise, W would be negative in the metal and lead to incorrect results when integrating over the full plasmonic volume.[4]

The effective mode volume is obtained by integrating the energy density over the volume of the nanoplasmonic structure, and normalizing it to the maximum value of $W(\boldsymbol{r})$ at each ω (which in our NPoM system around the plasmonic resonance always occurs at the centre of the gap and is always real):

$$V(\omega) = \frac{\int W(\boldsymbol{r},\omega)d^3\boldsymbol{r}}{\max[W(\boldsymbol{r},\omega)]} \tag{S3}$$

We note that $W(\boldsymbol{r},\omega)$ is complex inside the metal, since ε in metals is complex, and therefore $V(\omega)$ is complex. Here $\Re e(V)$ and $\Re e(W)$ are associated with the radiative channel of the system, and $\Im m(V)$, $\Im m(W)$ with the non-radiative channel (i.e. energy dissipation in the metal)[4] although $\Im m(V)$ is commonly neglected. This equation reduces to

the general definition of the mode volume $V = \frac{\int \varepsilon(\boldsymbol{r})|E(\boldsymbol{r})|^2 d^3\boldsymbol{r}}{\varepsilon(\boldsymbol{r_0})|E(\boldsymbol{r_0})|^2}$ only for lossless and dispersion-less dielectric cavities. In a magnetically dispersive, we note the second term of (S2) should be $\frac{\partial[\,\omega\,\mu(\boldsymbol{r},\omega)]}{\partial\omega}\,\mu_0\,\,|H(\boldsymbol{r},\omega)|^2$.

Numerical results:

To obtain an accurate value for $\int W(\boldsymbol{r},\omega)d^3\boldsymbol{r}$, the electric and magnetic fields need to be calculated in a 3D volume, and then integrated. The same geometry is used is as for Method I above. The accuracy of the simulations dramatically affects the value of $V(\omega)$. The most accurate results obtained are shown in Fig.S7, and use 0.3nm meshing (as for the dipole excitation above) with integration over the volume 82.5 x 82.5 x 68.4nm. The effective mode volume is minimum at $\lambda_V = 655.1$nm giving $V = 35.7 + i\,15.0$ nm^3, with the scattering and absorption cross-sections peaked at $\lambda_{\text{scat}} = 659.4$ nm and $\lambda_{\text{abs}} = 655.4$ nm (shown in Fig.S7b).

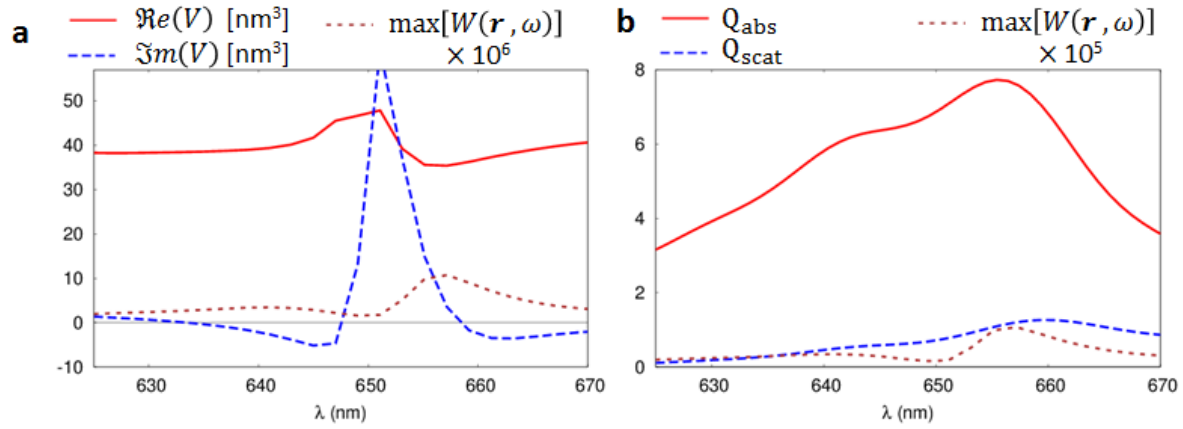

Figure S7 | Effective cavity volume. a, Extracted complex effective cavity volume from equation (S2), showing real and imaginary components and the maximum energy density. (b) Scattering and absorption cross-sections with maximum field enhancement in the gap.

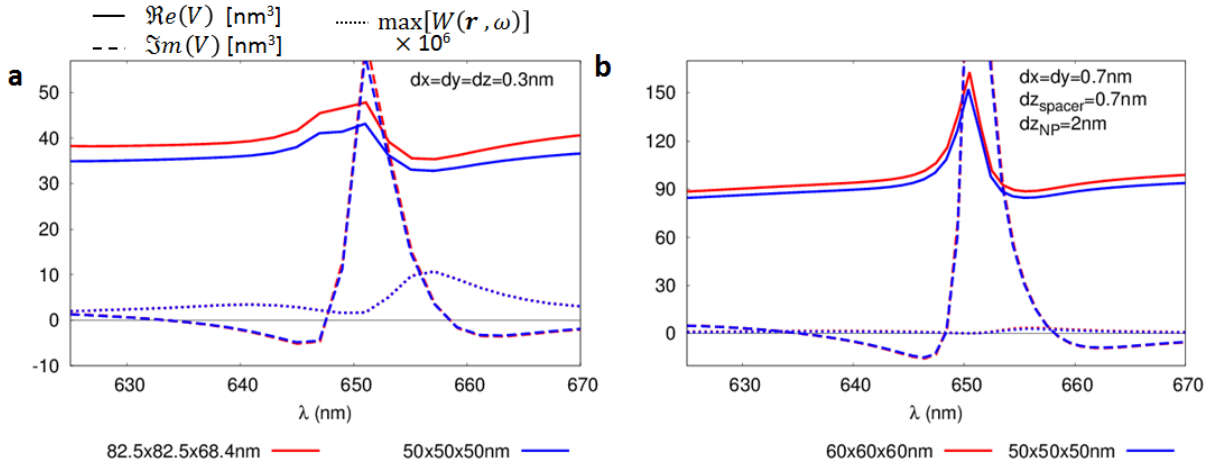

Figure S8 | Effect of meshing on cavity volume. a, Meshing dx=dy=dz=0.3nm, (b) meshing dx=dy=dz=0.7nm in the spacer and dx=dy=0.7nm, dz=2nm for the rest of the nanoparticle. Full lines are $\Re$e(V), dashed lines $\Im$m(V) and dotted lines are max[W(ω)].

The strong impact of the integral truncation and simulation meshing on the estimated mode volume can be seen from Figure S8. At the computationally-intensive converged level used in Fig.S8(a) we capture most of the radiative energy from the nanoparticle - increasing the integrated volume from blue to red lines changes the effective volume only slightly. If quicker simulation times are used (Fig.S8b) the meshing is not sufficient to converge and the effective mode volume is overestimated by at least one order of magnitude. Additionally, a small increase in the size of the gap (for example by 0.5nm) can increase the effective mode volume value by one order of magnitude.

We note that since most of the field $|E(\boldsymbol{r})|$ and energy density are confined only in the gap between the nanoparticle and mirror (Fig.S9), the permittivity $\varepsilon(r)$ is still dominated by the refractive index of the spacer layer in the gap. For 40, 50 and 60 nm particle sizes, V is found to be 23, 32 and 35 nm^3, respectively. As expected this scales with the predicted[5] lateral size of the NPoM gap mode, $V \simeq d\left(\sqrt{Rd}\right)^2 = d^2R$.

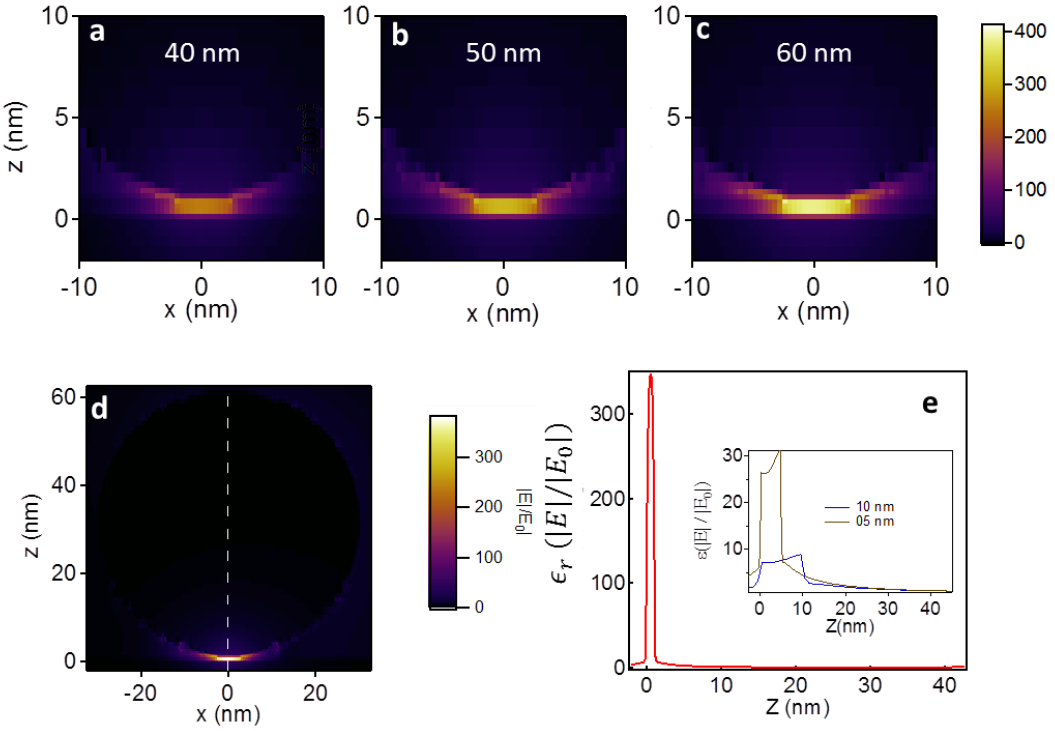

Figure S9| Calculation of mode volume (V). (a-c) FDTD simulated near-field images of NPoM at $\boldsymbol{\omega_{pl}}$ with increasing nanoparticle size (40-60 nm), used for calculating mode volume (V). (e) The line profile of $\epsilon_r|E|$ for 60 nm nanoparticle with 1 nm gap, taken along the dotted white line shown in (d). Similar line profiles for 5 nm and 10 nm gaps are shown in the inset.

The small mode volume here is directly related to the NPoM geometry, which confines plasmons almost completely into the dielectric region in between the metal surfaces. The reason for this is that the gap construct can be considered as a metal-insulator-metal (MIM) waveguide, and the lowest waveguide mode has extremely high in-plane wavevector[2], corresponding to effective refractive indices of up to 100. The resulting imaginary out-of-

plane wavevector ($k_\perp^2 = k_0^2 - k_\parallel^2$) is thus also very large, giving an extremely fast spatial decay into the metal, strongly confining the light inside the gap. We plot the enhanced optical field taken along a cross-section through the centre of the gap, with z=0 at the lower mirror surface (Fig.S9e) showing this for 1nm, 5nm, and 10nm gaps and revealing how in small gaps the field retracts from the metal.

We note recent hints of strong coupling effects in the tentative data of [S16]. While their cavity volumes were estimated to be 200 nm^3, we show from the above that this is likely a numerical convergence issue and sub-50nm^3 volumes are more likely. The estimated coupling g was 200 meV in this paper, however we find a number of erroneous numerical and conversion factors, and instead obtain 25meV for their parameters.

Calculation of mean number of molecules

Our previous[7] measurements on the number of molecules within the field volume of the NPoM geometry estimated 176 close-packed biphenyl-4,4'-dithiol self-assembled molecules under 60 nm nanoparticles. This corresponds to an area of 35 nm^2, which is similar to the mode volume that we calculated above.

The mean number of MB (dye) molecules within the mode volume is estimated from the geometry of CB[7] molecules in the same mode volume. The surface density of CB[7] self-assembled monolayer[8] is 2.41×10^{13} molecules cm^{-2}. This corresponds to an average of 104 CB[7] molecules in the mode volume under 40 nm nanoparticle in NPoM geometry. Given the molar ratio of CB[7]:MB (10, 7.5, 5 and 2.5), the mean number of MB molecules is estimated to be 10, 7.5, 5 and 2.5 respectively.

S7: Strong coupling parameters

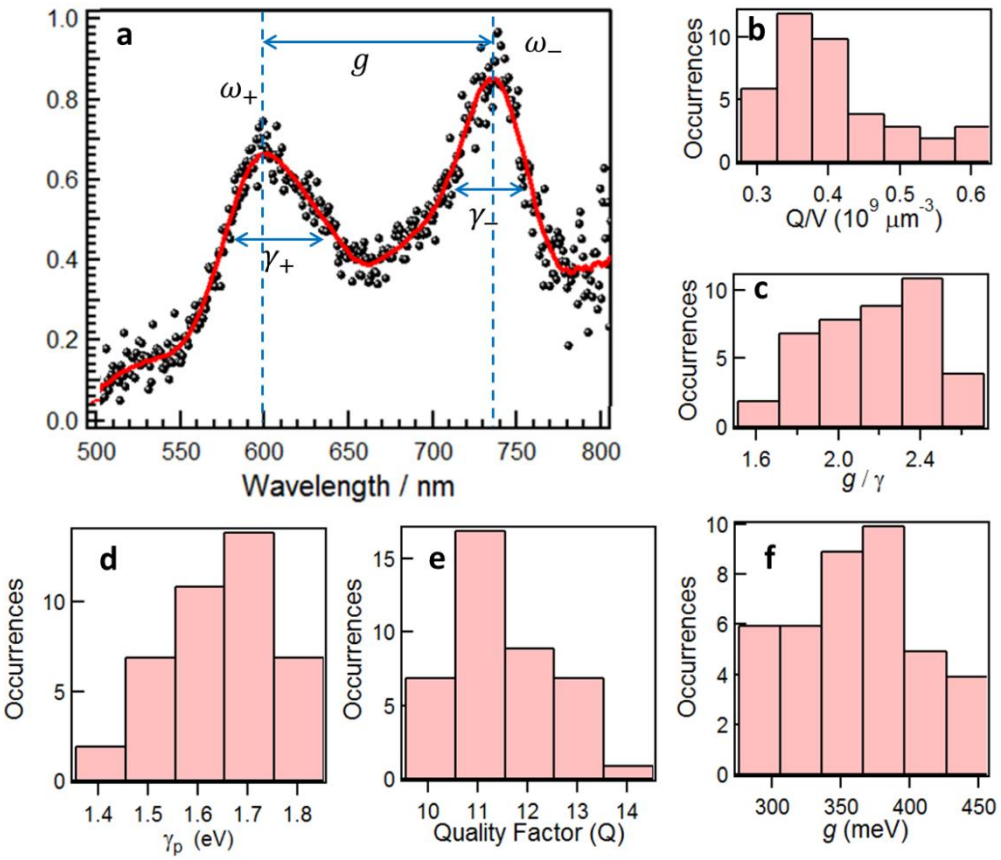

Figure S10 | Distribution of single-nanoparticle parameters extracted using the coupled oscillator model. a, Experimentally obtained scattering spectrum from NPoM geometry with MB+CB[7] sample, resulting in scattering dip at ω_0. The hybrid exciton-plasmon branches ($\omega_+$and ω_-) are separated by g. **b,c,** Occurrences of Q/V and g/γ for nanoparticles of different diameters used in the experiment, respectively. **d-f,** Occurrences of plasmon frequency, quality factor and coupling strength.

S8: Analytical fit for single-molecule coupling strengths

The electric field profile within the mode volume$|\boldsymbol{E}(\boldsymbol{r})|$, is extracted from the numerical FDTD results (Figure S9). To fit the experimental data for the single-molecule coupling strength when the molecules are distributed randomly (Figure 3b), values of $|\boldsymbol{E}(\boldsymbol{r})|$ are selected at different random in-plane spatial locations and used to generate the expected local coupling strengths (dashed line). Similarly for $n = 2 - 5$ molecules, multiple randomly selected spatial locations are used to select $|\boldsymbol{E}(\boldsymbol{r})|$ which then provide the estimated range of coupling strengths.

S9: SERRS + PL in strong and weak coupling regime

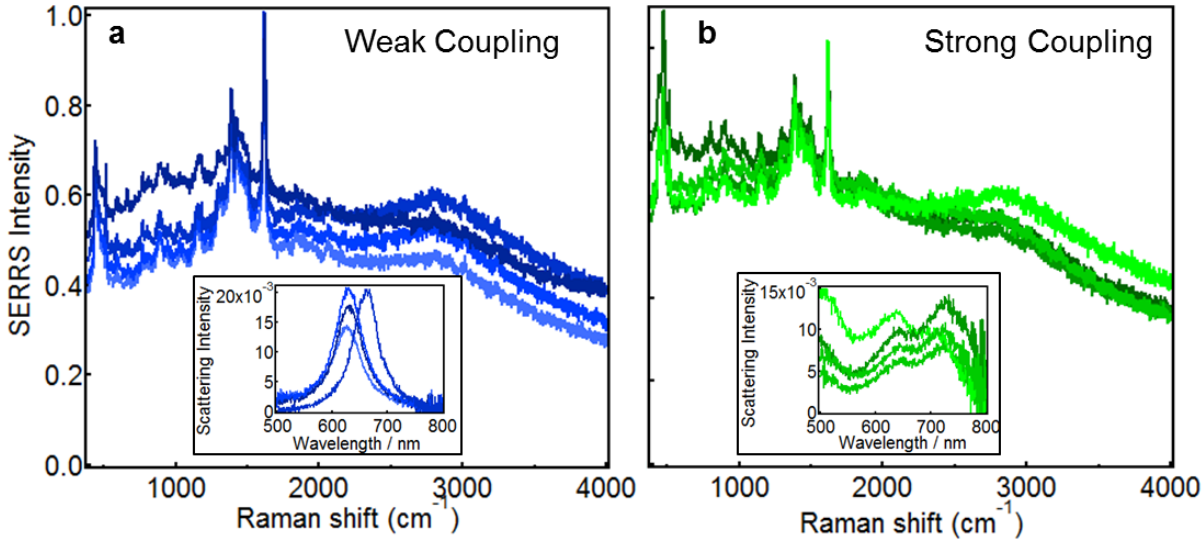

Figure S11 | SERRS + PL from single-nanoparticle in strong and weak coupling regimes. a,b, Emission spectrum obtained from dye molecules in gap-mode of single-nanoparticles, illuminated with 633 nm laser in **a**, weak and **b**, strong coupling regimes. Insets show simultaneous dark-field spectra on the same NPoMs. Main text shows expanded region around 480 cm^{-1}.

S10: Quantum Efficiency

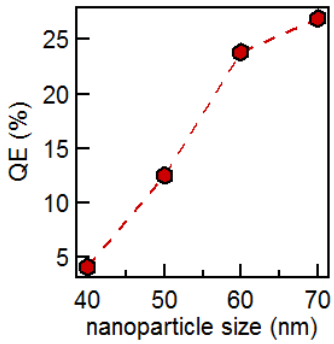

Figure S12 | Quantum efficiency. Numerically simulated outcoupling efficiencies for vertical dipole placed at the centre of NPoM gap with nanoparticle of different diameters.

S11: Single vs few molecule coupling

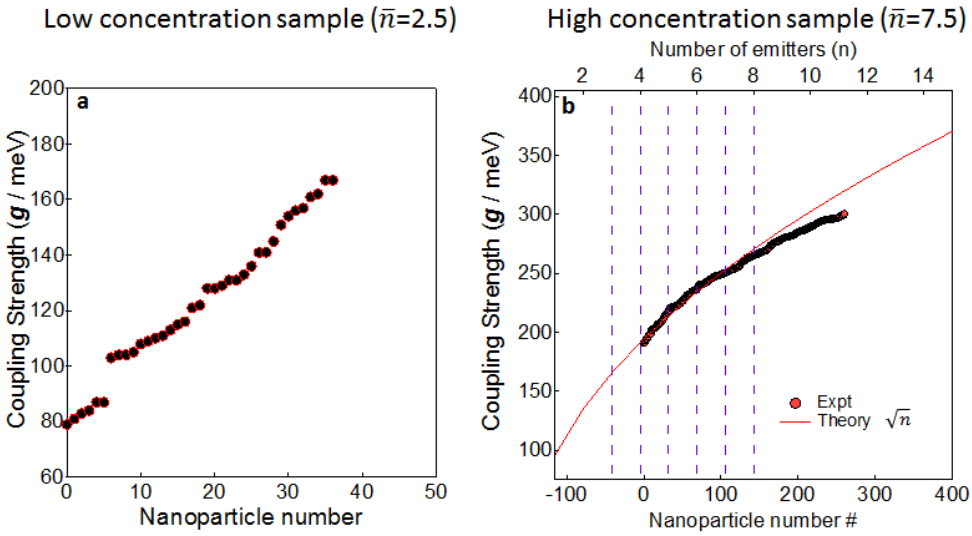

Figure S13 | Single- vs few-molecule coupling strengths. Coupling strength extracted from several different NPoM samples (repeating those in the main text) of (a) $\bar{n} = 2.5$ and (b) $\bar{n} = 7.5$. In the latter case, there are always many molecules for each NPoM junction, and their different positions leads to washing out of the jumps seen in (a). Also plotted is the theoretical dependence on $\sqrt{n}$, although the data averages over the distribution of molecule numbers and their lateral positions within the gap.

S12: Semi-quantum model for strong coupling

The dynamics of a two-level quantum emitter may be described by its corresponding density matrix ρ. The optical Bloch equations describe in mathematical form the coupling between a classical electric field $\boldsymbol{E}$ and the diagonal (1) and off-diagonal (2) elements of the density matrix ρ of the two level quantum system:

$$\frac{\partial \rho_{12}}{\partial t} = \frac{\partial \rho_{21}^*}{\partial t} = -(i\omega_r + \Gamma)\rho_{12} - i\frac{\boldsymbol{\mu}.\boldsymbol{E}}{\hbar}(\rho_{22} - \rho_{11}) \quad (1)$$

$$\frac{\partial \rho_{22}}{\partial t} = -\frac{\partial \rho_{11}}{\partial t} = i\frac{\boldsymbol{\mu}.\boldsymbol{E}}{\hbar}(\rho_{12}^* - \rho_{21}) = 2\frac{\boldsymbol{\mu}.\boldsymbol{E}}{\hbar}Im(\rho_{12}) \quad (2)$$

where ω_r is the transition resonance frequency between the two energy levels, Γ accounts for the decoherence of the polarisation ρ_{12}, and $\boldsymbol{\mu}$ is the dipole matrix element of the electronic transition.

The incident classical electric field $\boldsymbol{E}$ interacts with the inversion $\rho_{22} - \rho_{11}$ which drives the polarisation ρ_{12} via equation (1). The polarisation in turn couples to the electric field to drive the inversion via equation (2). Meanwhile the electric field depends on the polarisation via the Maxwell equations, where the macroscopic polarization $\boldsymbol{P}$ is given by

$$\boldsymbol{P} = N\boldsymbol{\mu}(\rho_{12} + \rho_{21}), \quad (3)$$

and N is the number of quantum emitters.

In the semi-classical/semi-quantum simulations, equations (1-3) are solved at each point in space and time and self-consistently coupled with Maxwell's equations (not shown) integrated with an FDTD algorithm. We obtain the characteristic mode splitting (Fig.S14) for the NPoM geometry for both 90° and 0° field incidence, and show the mode splitting $\Delta\lambda$ in both cases to be proportional to $\sqrt{N/V}$ in accordance with strong coupling theory.

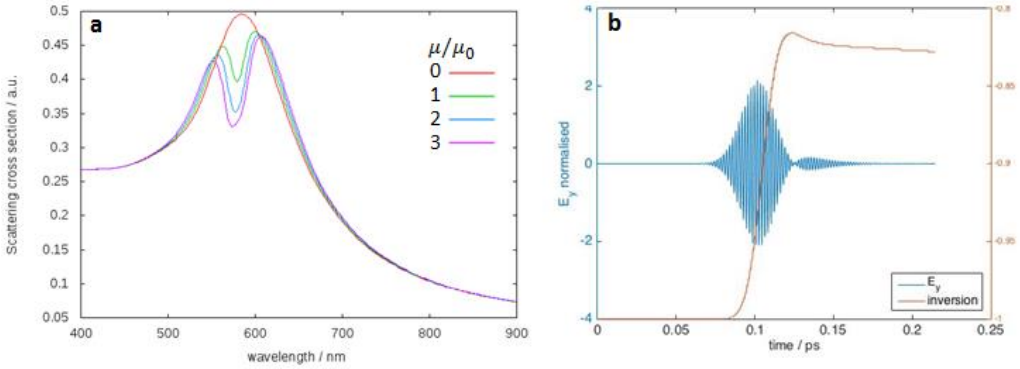

Figure S14 | Semi-quantum model for strong coupling. a, Scattering spectra with and without quantum emitters in the NPoM geometry. Density of quantum emitters in the gap is varied, showing expected increase in Rabi splitting. **b**, Time variation of electric field in the gap, showing Rabi oscillation.

S13: Single-molecules via bianalyte SERS - analogue of $g^{(2)}$

We cannot yet use conventional methods to prove single photon emission, so for now we use a single molecule route to verify $g^{(2)}$. We adopt the bianalyte method which has been well-studied and well-proven in chemistry for confirming surface-enhanced Raman scattering (SERS) of single molecules[9–12]. The principle is to use two molecules with well-distinguished Raman spectra, and show that mixtures at low concentrations give signals which arise from one or the other, but not both molecules.

We use provflavine (PF) as a second molecule which is very similar chemically and structurally to methylene blue (MB), and binds inside CB[7] in the same way at the concentration of 0.2 dye per 100 nm size nanoparticle. However MB and PF can be easily distinguished in the 400-460cm^{-1} region (Fig.S15a,b). The SERS of low concentration 50:50 mixtures are measured for >500 NPoMs, and the data analysed using principal component analysis which finds the most distinguishable spectral components (Fig.S15d). At this concentration where $\bar{n} = 0.2$, the lowest two eigenmodes indeed dominate, corresponding to each molecule alone (Fig.S15e). This allows us to construct a histogram (Fig.S15f, Fig.4f) which gives the probability that the two molecular spectra are detected simultaneously in different fractions (right end corresponds to 100% MB, left to 100% PF).

As clearly evident, at these lowest concentrations we find that two molecules are almost never found at the same time, and we are truly in the single molecule regime. We can use this data to construct a 'chemical' $g_{ch}^{(2)}$, defined as the probability of detecting two different molecules at the same time normalised by the probability of finding them both at 100% filling of the CBs (ie. with all the CBs in the NPoM junction filled with either molecule). We find $g_{ch}^{(2)}$~0.3, much less than 1, which provides strong evidence that we see strong coupling with single molecules. Similar histograms at higher concentrations show the gradual washing out of single-molecule signatures (Fig.S16).

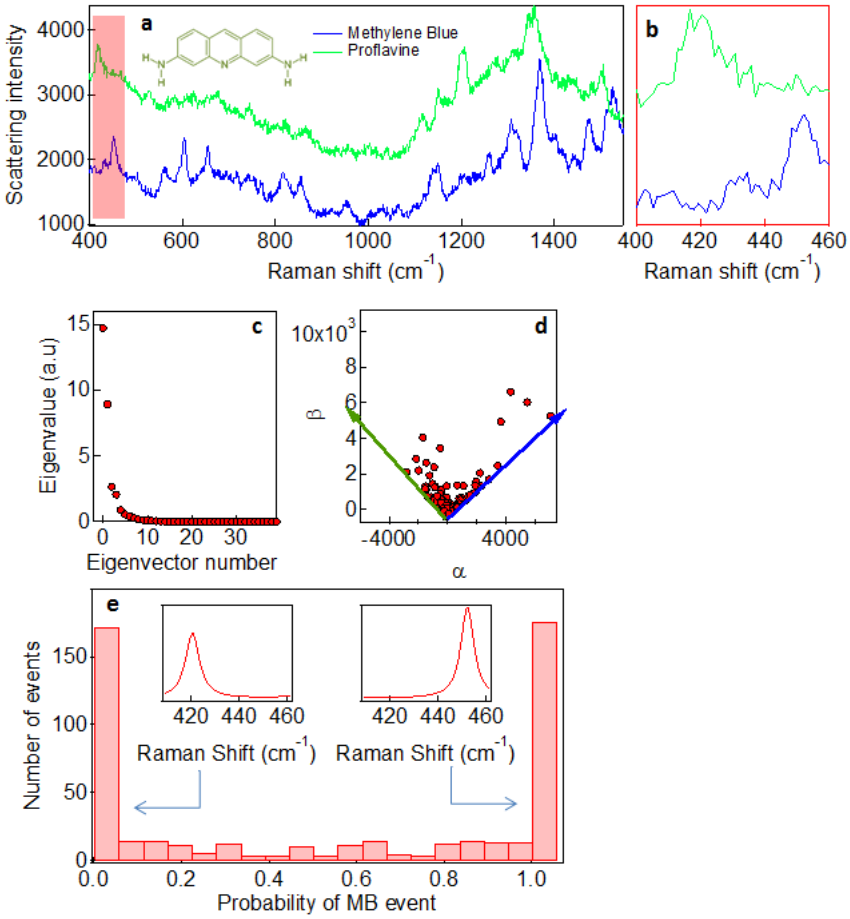

Figure S15 | PCA analysis for bi-analyte SERS. a, SERS spectra from methylene blue (MB) and provflavine (PF, inset) molecules collected in NPoM geometry with an integration time of 2 s and with excitation at 785 nm. **b**, Selected wavenumbers in which MB and PF show distinct Raman peaks. **c,** SERS for more than 500 nanoparticles from NPoM geometry at the concentration of 1:100 (dye:CB) ratio, which gives $\bar{n} = 0.2$ dye molecules per nanoparticle. This data was processed with rigorous modified principal component analysis (MPCA)[12], to obtain covariance matrix and extract eigenvalues shown**. d**, The coefficient matrix denotes the distribution of the dye signals which are distinguished from each other along the two orthogonal axis indicated through blue and green arrows. **e,** Single-molecule probability histogram derived from MPCA analysis. Inset shows the signature of the two different probabilities.

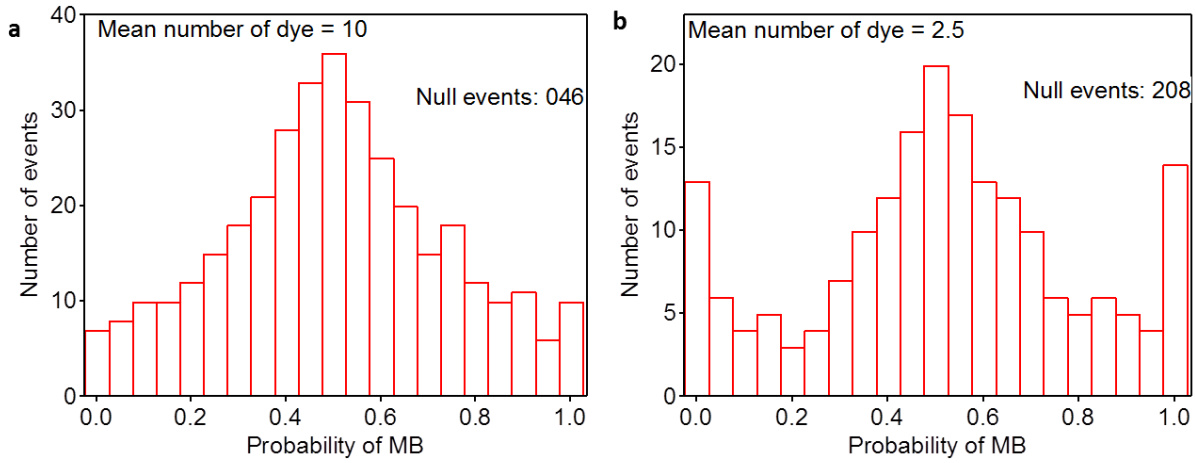

Figure S16 | PCA analysis for bi-analyte SERS at different concentrations. a,b, Probability histograms derived from MPCA analysis for $\bar{n} = 10$ and $\bar{n} = 2.5$ dyes per nanoparticle respectively.

To compare with the experiments in the main text Figure 4, for several different average numbers of dye molecule per nanoparticle, we tabulate in Fig.S17 the number of nanoparticles that we find in SERS show single molecule scattering (see below) compared also to the number we find in dark field scattering from the Rabi splitting, as well as the levels that would be expected from Poissonian statistics, $p_k = \bar{n}^k e^{-\bar{n}}/k!$. For $\bar{n} = 10$ as expected most nanoparticles seem to give more than one dye molecule, although we note a 20% background of nanoparticles which still do not show a discernable Rabi splitting (likely caused by incorrect nano-geometry or tuning). For $\bar{n} = 2.5$ we see the same excess of n=0 nanoparticles both in SERS and dark-field, however the fraction which show single molecules is within a factor of 2 of the theory prediction. When we reduce the density of MB still further to $\bar{n} = 0.2$ the anticrossing is so infrequent that we were not able to collect robust statistics (very long timescales are required for these measurements), however again the SERS statistics matches quite well the prediction (fitting $\bar{n} = 0.4$ even better).

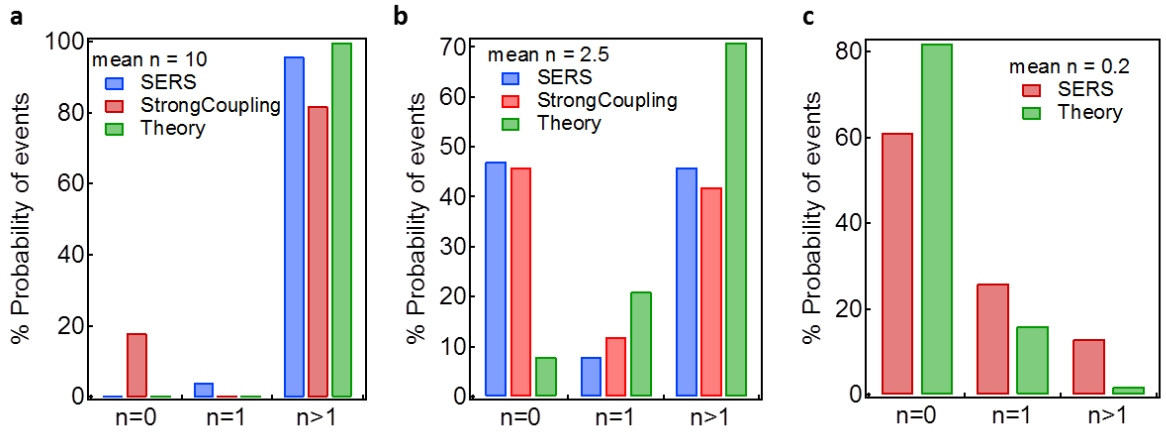

Figure S17 | Statistics of single-molecule events from different experimental methods. Statistics of null events, single-molecule events, and few molecule events are compared from bi-analyte SERRS and strong-coupling scattering experiments with theoretical predictions, for **a,** $\bar{n} = 10$, **b,** $\bar{n} = 2.5$, and **c,** $\bar{n} = 0.2$.

This suggests the effective MB concentrations that are found under the nanoparticles differ slightly from those expected by dilution, though are similar within a factor of two.

S14: Spectral diffusion of single-molecule SERRS

We record time-series SERRS spectra from nanoparticles exhibit strong coupling in this single-molecule n=1 regime (see main text). The Raman pump laser is at 633nm. From the time-series scans (Fig.S18a, Fig.S19) we observe clear spectral diffusion of the vibrational peaks of single MB molecules. Such spectral diffusion is well-studied well-proven evidence of single-molecule events both in the fluorescence community[13,14] and the SERS community[15,16]. The vibrational shifts for different bonds are seen to be correlated but can be in opposite directions, which is only possible to account for if they are from individual molecules. This confirms the presence of single molecules which leads to strong coupling at room temperature. This is completely different when comparing with gaps that are filled with many MB molecules (which is the case when no CBs are used, Fig.S18b), that shows no spectral wandering (averaging over many molecules) though some changes in intensity are seen as molecules sporadically reorient and match the optical field better.

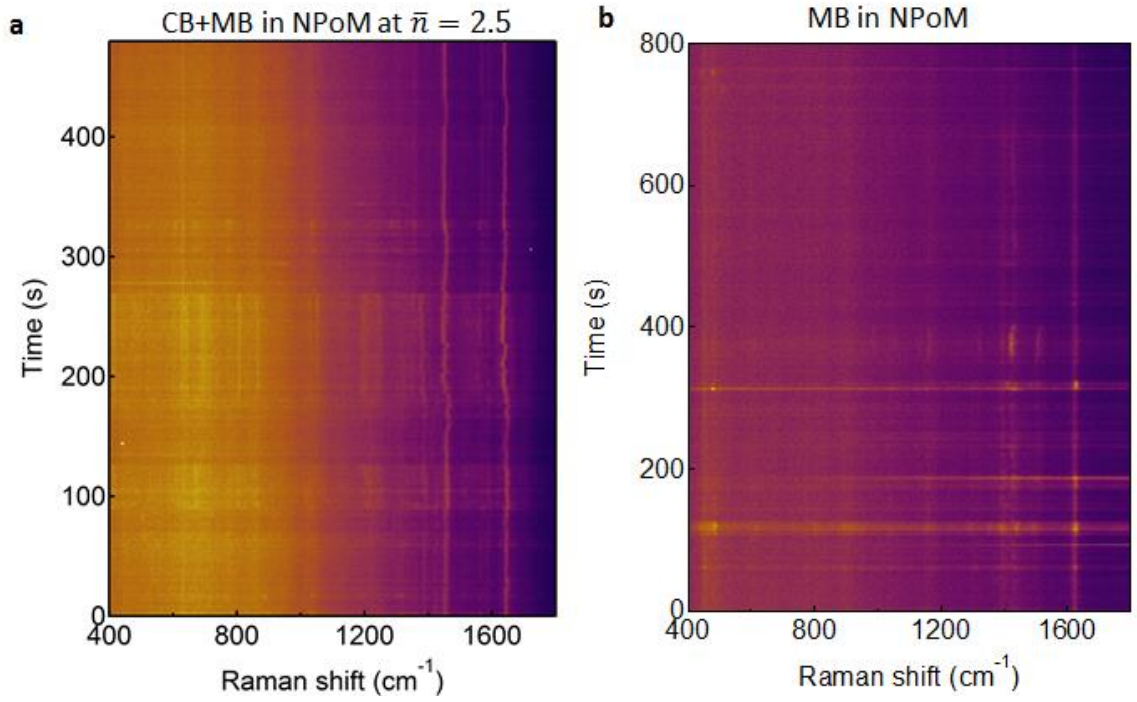

Figure S18 | Spectral diffusion of single-molecule SERRS. a, Time dependent evolution of SERRS signal from a CB+MB nanoparticle-on-mirror which exhibited the signature of single-molecule strong coupling in its scattering spectrum. Each SERS spectrum is collected for 2s. Spectral diffusion of vibrational lines of MB is clearly evident, with correlations in the different lines implying their single-molecule origin. **b,** Such spectral diffusion is not evident at higher concentrations with many MBs lying flat to the metal surface (which also gives weaker SERS coupling).

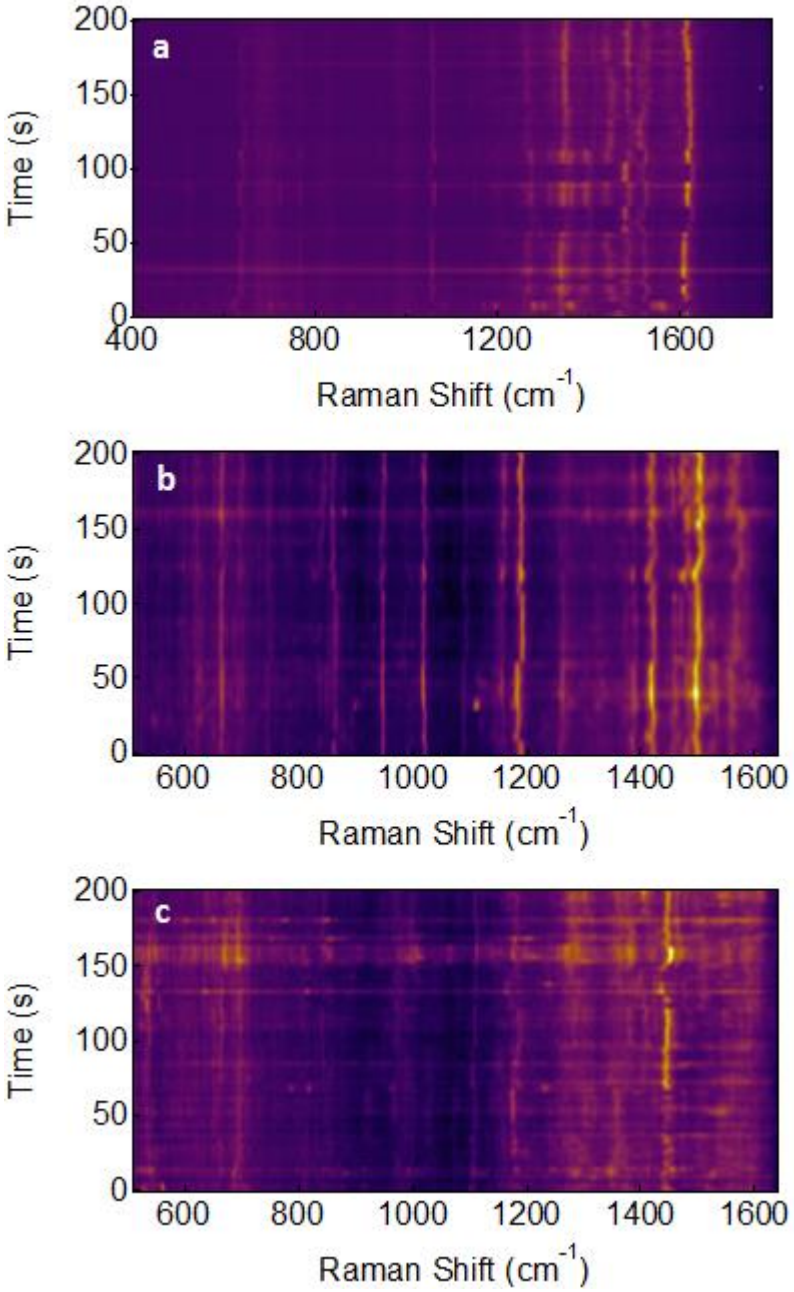

Figure S19 | Spectral diffusion of single-molecule SERRS from different NPoM. Time dependent evolution of SERRS signals from CB+MB nanoparticles, each exhibiting the signature of single-molecule strong coupling (Fig.4b, n=1). Each spectrum is collected for 2s. Spectral diffusion of vibrational lines of MB is clearly evident and is observed from all of the different NPoM constructs.

S15: Single-molecule anticrossing

We use a sample in which a mixture of nanoparticle sizes from 35-45nm diameter is now used, thus providing NPoM plasmon resonances which tune around the emission line of the MB molecules. Again extracting those NPoM which show splitting in the n=1 regime, we can construct a detuning dispersion as shown in Fig.S20. These again fit the same expected anticrossing dispersion.

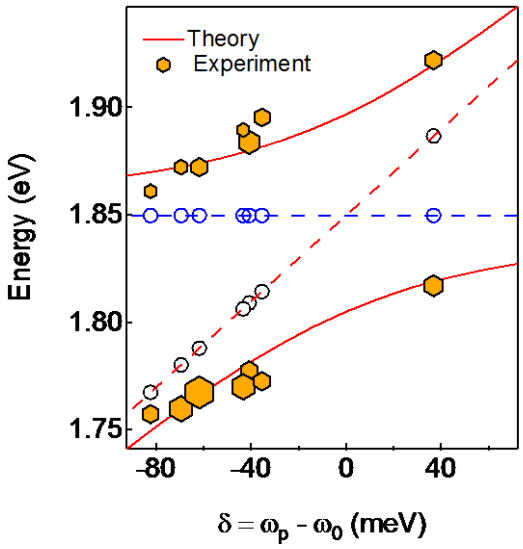

Figure S20 | Single-molecule anticrossing. Spectra exhibiting two coupled resonance in the single-molecule regime n=1 of Figure 4 for different nanoparticle size (40-60 nm) are extracted and plotted as function of detuning. Resonance position of lower and upper plexciton mode is fit with the coupled oscillator model.

References

1. Feist, J. & Garcia-Vidal, F. J. Extraordinary exciton conductance induced by strong coupling. *Phys. Rev. Lett.* **114,** (2015).
2. Sigle, D. O. *et al.* Monitoring Morphological Changes in 2D Monolayer Semiconductors Using Atom-Thick Plasmonic Nanocavities. *ACS Nano* **9,** 825–830 (2015).
3. Tszerkis. *Phys. Rev. B* **in press,** (2015).
4. Sauvan, C., Hugonin, J. P., Maksymov, I. S. & Lalanne, P. Theory of the Spontaneous Optical Emission of Nanosize Photonic and Plasmon Resonators. *Phys. Rev. Lett.* **110,** 237401 (2013).
5. Savage, K. J. *et al.* Revealing the quantum regime in tunnelling plasmonics. *Nature* **491,** 574–577 (2012).
6. Itoh, T. *et al.* Single-molecular surface-enhanced resonance Raman scattering as a quantitative probe of local electromagnetic field: The case of strong coupling between plasmonic and excitonic resonance. *Phys. Rev. B* **89,** 195436 (2014).
7. Benz, F. *et al.* Nanooptics of Molecular-Shunted Plasmonic Nanojunctions. *Nano Lett.* **15,** 669–674 (2015).
4. An, Q. *et al.* A general and efficient method to form self-assembled cucurbit[n]uril monolayers on gold surfaces. *Chem. Commun.* **17,** 1989–1991 (2008).

9. Etchegoin, P. G., Ru, E. C. L. & Fainstein, A. Bi-analyte single molecule SERS technique with simultaneous spatial resolution. *Phys. Chem. Chem. Phys.* **13,** 4500–4506 (2011).
10. Le Ru, E. C., Meyer, M. & Etchegoin, P. G. Proof of Single-Molecule Sensitivity in Surface Enhanced Raman Scattering (SERS) by Means of a Two-Analyte Technique. *J. Phys. Chem. B* **110,** 1944–1948 (2006).
11. Patra, P. P. & Kumar, G. V. P. Single-Molecule Surface-Enhanced Raman Scattering Sensitivity of Ag-Core Au-Shell Nanoparticles: Revealed by Bi-Analyte Method. *J. Phys. Chem. Lett.* **4,** 1167–1171 (2013).
12. Patra, P. P., Chikkaraddy, R., Tripathi, R. P. N., Dasgupta, A. & Kumar, G. V. P. Plasmofluidic single-molecule surface-enhanced Raman scattering from dynamic assembly of plasmonic nanoparticles. *Nat. Commun.* **5,** (2014).
13. Ambrose, W. P. & Moerner, W. E. Fluorescence spectroscopy and spectral diffusion of single impurity molecules in a crystal. *Nature* **349**, 225-227 (1991).
14. Reilly, P. D. & Skinner, J. L. Spectral diffusion of single molecule fluorescence: A probe of low-frequency localized excitations in disordered crystals. *Phys.Rev.Lett.* **71**, 4257-4260 (1993).
15. Shuming, N. & Emory, S. R. Probing Single Molecules and Single Nanoparticles by Surface-Enhanced Raman Scattering. *Science* **275**, 1102-1104 (1997).
16. Neacsu, C. C., Dreyer, J., Behr, N., and Raschke, M.B. Scanning-probe Raman spectroscopy with single-molecule sensitivity. *Phys.Rev.B* **73**, 193406 (2006).